
Article:
Asiri, F., Ballai, I. orcid.org/0000-0002-3066-7653, Fedun, V. et al. (3 more authors) (2024) Slow body magnetohydrodynamic waves in solar photospheric flux tubes with density inhomogeneity. Monthly Notices of the Royal Astronomical Society, 529 (1). pp. 748-760. ISSN 0035-8711

https://doi.org/10.1093/mnras/stae497

Monthly Notices of the ROYAL ASTRONOMICAL SOCIETY

MNRAS **529,** 748–760 (2024) https://doi.org/10.1093/mnras/stae497
Advance Access publication 2024 March 1

Slow body magnetohydrodynamic waves in solar photospheric flux tubes with density inhomogeneity

F. Asiri,[1,2]★ I. Ballai,[1] V. Fedun,[3] G. Verth,[1] S. N. Ruzheinikov[3] and A. B. Albidah[4]

[1]*Plasma Dynamics Group, School of Mathematics and Statistics, The University of Sheffield, Hicks Building, Hounsfield Road, Sheffield S3 7RH, UK*
[2]*Department of Mathematics, College of Science, Taibah University, Madinah, Saudi Arabia*
[3]*Plasma Dynamics Group, Department of Automatic Control and Systems Engineering, The University of Sheffield, Sheffield S1 3JD, UK*
[4]*Department of Mathematics, College of Science Al-Zulfi, Majmaah University, Al-Majmaah 11952, Saudi Arabia*

Accepted 2024 February 7. Received 2024 February 5; in original form 2023 December 15

ABSTRACT

Pores and sunspots are ideal environments for the propagation of guided magnetohydrodynamic (MHD) waves. However, modelling such photospheric waveguides with varying background quantities such as plasma density and magnetic field has thus far been very limited. Such modelling is required to correctly interpret MHD waves observed in pores and sunspots with resolved inhomogeneities such as light bridges and umbral dots. This study will investigate the propagation characteristics and the spatial structure of slow body MHD modes in a magnetic flux tube with a circular cross-section with inhomogeneous equilibrium density distribution under solar photospheric conditions in the short wavelength limit. For simplicity, the equilibrium density profile is taken to have a circular density enhancement or depletion. The advantage of this is that the strength, size, and position of the density inhomogeneity can be easily changed. Calculating the eigenfrequencies and eigenfunctions of the slow body modes is addressed numerically with use of the Fourier–Chebyshev Spectral method. The radial and azimuthal variation of eigenfunctions is obtained by solving a Helmholtz-type partial differential equation with Dirichlet boundary conditions. The inhomogeneous equilibrium density profile results in modified eigenvalues and eigenvectors. It was found that a localized density inhomogeneity leads to a decrease in the eigenvalues and the spatial structure of modes ceases to be a global harmonic oscillation, as the modes migrate towards regions of lower density. Comparing the homogeneous case and the cases corresponding to depleted density enhancement, the dimensionless phase speed undergoes a significant drop in its value (at least 40 per cent).

Key words: waves – Sun: oscillations – Sun: photosphere – sunspots.

1 INTRODUCTION

High-resolution observations in the last few decades confirm that the solar atmosphere is filled with magnetohydrodynamic (MHD) waves (Mathioudakis, Jess & Erdélyi 2013; Jess et al. 2015; Li et al. 2020; Banerjee et al. 2021; Jess et al. 2023, to name but a few). Waves are natural manifestations of disturbances in the solar plasma when deviations in the equilibrium state of the plasma are paired with various restoring forces that tend to restore the equilibrium state. MHD waves have been extensively studied in connection to plasma heating or acceleration (see e.g. Erdélyi & Ballai 2007; De Moortel & Browning 2015; Van Doorsselaere et al. 2020; Li et al. 2022 and references therein), and as a diagnostic tool using magneto-seismological techniques that aim to determine the plasma and field parameters that cannot be measured directly or indirectly (for a few reviews see, e.g. Nakariakov et al. 1999; Ballester 2005; Verth 2007; Ballai 2007; Oliver 2009; De Moortel & Nakariakov 2012).

In general, seismological techniques involve a close comparison of theoretical models (dispersion relations, evolutionary equations) with determined wave parameters from observations (amplitude, decay time/length, wavelength, propagation speed, etc.). Often MHD waves are observed to follow the direction of the magnetic field (these waves are labelled as guided waves), meaning that waves can also be used as tracers of the magnetic field. While observations have their own limitations driven by the existing temporal and spatial resolution, these helped to understand various physical phenomena and to build up connectivity relationships between several important features in the solar atmosphere. At the same time, most of the existing theoretical models operate with a high degree of idealization. Waves propagating along the magnetic field are confined to magnetic structures that are modelled as straight and homogeneous structures with their cross-section being a regular shape (mostly circular). In reality, observations show that magnetic waveguides are far from having a regular cross-section and being homogeneous either in the radial or longitudinal direction. Inhomogeneities in the plasma and magnetic field are known to strongly influence the properties of waves, leading to the modifications in the spectral properties of waves, wave amplification, mode conversion, etc. (e.g. De Pontieu et al. 2007; Morton et al. 2011; Aldhafeeri et al. 2021, 2022; Skirvin et al. 2022; Stangalini et al. 2022 to name but a few).

Pores and sunspots are probably the most studied magnetic features in the lower solar atmosphere and they are the location of emerging large-scale kG magnetic field whose transverse shape

★ E-mail: fahasiri1@sheffield.ac.uk

and area change over time (Forgács-Dajka, Dobos & Ballai 2021). Pores are located often along the dividing lines between larger sunspots and smaller magnetic elements. A particular manifestation of inhomogeneities in pores and the umbral region of sunspots are regions of limited extent called umbral dots (UDs) and light-bridges (LBs) that are luminous regions that separate the umbra of a sunspot and indicate sunspot decay or fragmentation, (Garcia de La Rosa 1987). They are believed to play an important role in the energy balance in sunspots and pores (Solanki 2003). LBs can be thought of as large-scale magneto-convection manifestations in umbrae (Rimmele 2008). The fine structure and energy transmission in sunspots are now mostly, if not completely, attributed to the latter hypothesis. There is hardly any part of the umbra which does not support UDs. They account for about 11 per cent of the umbral area (Riethmüller et al. 2008) and 10–20 per cent of its brightness (Yadav, Louis & Mathew 2018). The majority of UDs appear to form close to the edge of the umbra and subsequently migrate towards the sunspots' centre at velocities of about 700 m s^{-1} (Watanabe 2014). UDs have a lifetime ranging from 2.5 to 10 min (Riethmüller et al. 2008; Watanabe, Kitai & Ichimoto 2009; Louis et al. 2012). Based on their location, UDs are divided into central and peripheral dots. The magnetic fields of the peripheral UDs are weaker (and inclined) and they appear brighter than those situated in the centre. According to Watanabe et al. (2009), UDs appear when the magnetic field is weaker and inclined and disappear where it is the field becomes stronger and vertical. Using Hinode blue-continuum observations, Watanabe (2014) found that, as sunspots progress, UDs become less dense and more clumped together. Ji et al. (2016) employed New Vacuum Solar Telescope observations to show that the lifetime of UDs located in several sunspots were correlated with the strength of the accompanying magnetic fields. They also found that the effective diameter, intensity, and velocity are affected by the fluctuation in the magnetic field. Yadav, Mathew & Tiwary (2017) performed a statistical comparison of the properties of UDs using Hinode observations of seven sunspots seen in high-resolution, G-band continuum filtergrams and they found that the average effective diameter of UDs is 270 km. Magnetoconvection numerical simulations using the MURaM code by Schüssler & Vögler (2006) have shown that UDs are the result of narrow, upflowing, convective plumes with adjacent downflows. The physical parameters of UDs using high resolutions observational data were studied in great detail by, e.g. Feng et al. (2015), Yadav et al. (2017), Kilcik et al. (2020), etc. Inhomogeneities in the magnetic field and plasma composition can dramatically alter the propagation of waves and the energy carried by them (Henriques et al. 2020; Yuan et al. 2023).

The existence of waves and oscillations in sunspots has been extensively studied since Beckers & Tallant (1969)'s pioneering work demonstrated the oscillatory behaviour of sunspots by measuring observed parameters of umbral flashes. Beckers & Schultz (1972) detected three-minute oscillations in Doppler velocity in the umbral area. Subsequent studies have shown that the most significant oscillation periods in sunspots and pores are 5 min at photospheric heights and 3 min at chromospheric heights, while the periods of global sunspot oscillations vary from hours to days (Sekii et al. 2007; Stangalini et al. 2011; Jess et al. 2012; Grant et al. 2015; Jess et al. 2015; Khomenko & Collados 2015). In addition, Stangalini et al. (2021) demonstrated that, in contrast to the anticipated 5 min, the dominant oscillations of a magnetic pore observed with the Interferometric BIdimensional Spectropolarimeter (IBIS) have periods of 3 min in the photosphere. In contrast, studies involving numerous photospheric pores by Keys et al. (2018); Gilchrist-Millar et al. (2021); Grant et al. (2022) evidenced propagating waves with periods of 5 min.

This paper focuses on the analysis of modifications in the spatial structure and propagation speed of guided slow-body MHD waves due to the presence of an inhomogeneous equilibrium density distribution. The background of our investigation is based on the fact that slow body modes correspond to those perturbations for which the total pressure becomes almost zero near the boundary of the waveguide, as shown by Aldhafeeri et al. (2021), who demonstrated that in the case of slow body waves under photospheric conditions the dispersive character of waves and their properties can be confidently described by solving a Helmholtz equation with Dirichlet boundary condition, i.e. the total pressure perturbation vanishes at the boundary of the waveguide. This study has also showed that slow body waves in the solar photosphere considering the total pressure perturbation or the longitudinal component of the velocity perturbation zero at the boundary of the waveguide produces errors in eigenvalues that are less than 1 per cent from the values we would obtain by deriving the full dispersion relation. In our present investigations, we employ this result, as this approach considerably simplifies the analysis.

The paper is structured as follows: in Section 2 we derive the governing equations for an inhomogeneous waveguide assuming a constant plasma-β limit. This allows us to reduce our governing equation to a Sturm–Liouville eigenvalue problem. In Section 3 we present the Fourier–Chebyshev Spectral (FCS) method which is employed to solve the governing equation, with the details presented in the Appendix. The changes in the spatial structures of slow body modes and the modifications of the phase speed of waves on the parameters characterizing the plasma environment and density inhomogeneity, i.e. its position, size, strength, and the thickness of the transition region between regions of different densities is discussed in Section 4. Finally, our results are concluded and discussed in Section 5.

2 GOVERNING EQUATIONS

The dynamics of slow body waves will be discussed within the framework of ideal MHD and the equations that describe the spatial and temporal evolution of physical quantities are given by

$$\frac{\mathrm{D}\rho}{\mathrm{D}t} = \nabla \cdot (\rho \mathbf{u}), \tag{1}$$

$$\rho \frac{\mathrm{D}\mathbf{u}}{\mathrm{D}t} = -\nabla p + \frac{1}{\mu}\left[(\nabla \times \mathbf{B}) \times \mathbf{B}\right], \tag{2}$$

$$\frac{\mathrm{D}}{\mathrm{D}t}\left(p\rho^{-\gamma}\right) = 0, \tag{3}$$

$$\nabla \times (\mathbf{u} \times \mathbf{B}) = \frac{\partial \mathbf{B}}{\partial t}, \quad \nabla \cdot \mathbf{B} = 0, \tag{4}$$

where ρ is the plasma density, $\mathbf{u}$ is the velocity vector, p is the plasma pressure, $\mathbf{B}$ is the magnetic field, μ is the magnetic permeability of free space, and γ is the adiabatic index. In the above equations $\mathrm{D}/\mathrm{D}t = \partial/\partial t + \mathbf{u} \cdot \nabla$ is the total material derivative. Assuming small perturbations in the physical variables the above system of equations can be linearized by writing the physical quantities as the sum of their background (equilibrium) value (f_0) and a small perturbation (f) of the form $f_0 + f$. In this approximation every term containing the product of two perturbations becomes negligible. For the sake of simplicity, the equilibrium is considered as static.

We consider a straight magnetic cylinder with constant radius R and the dynamics will be described in cylindrical coordinates (r, θ, z). The constant equilibrium magnetic field, $\mathbf{B}_0 = B_0\hat{\mathbf{z}}$ is directed along the z-axis. The equilibrium plasma density profile inhomogeneity is

denoted by $\rho_0(r,\theta)$ and the components of the velocity and magnetic field perturbations are $\mathbf{u} = (u_r, u_\theta, u_z)$ and $\mathbf{b} = (b_r, b_\theta, b_z)$. The perturbed quantities can be Fourier decomposed with respect to the coordinate z and time, t, by writing them proportional to $e^{i(kz-\omega t)}$, where k is the longitudinal wave number and ω is the angular frequency. With these considerations the system of MHD equations (1)–(3) can be written as

$$-i\omega\rho + \rho_0\left[\frac{1}{r}\frac{\partial}{r}(ru_r) + \frac{1}{r}\frac{\partial u_\theta}{\partial\theta} + iku_z\right] + u_r\frac{\partial\rho_0}{\partial r} + \frac{u_\theta}{r}\frac{\partial\rho_0}{\partial\theta} = 0, \tag{5}$$

$$-i\rho_0\omega u_r = -\frac{\partial P_T}{\partial r} + ik\frac{B_0}{\mu}b_r, \tag{6}$$

$$-i\rho_0\omega u_\theta = -\frac{1}{r}\frac{\partial P_T}{\partial\theta} + ik\frac{B_0}{\mu}b_\theta, \tag{7}$$

$$\omega\rho_0 u_z = kP_T - k\frac{B_0}{\mu}b_z, \tag{8}$$

$$b_r = -B_0\frac{k}{\omega}u_r, \quad b_\theta = iB_0ku_\theta,$$

$$b_z = -iB_0\frac{1}{\omega r}\frac{\partial}{\partial r}(ru_r) - iB_0\frac{1}{\omega r}\frac{\partial u_\theta}{\partial\theta}, \tag{9}$$

$$p = -i\rho_0\frac{C_S^2}{\omega}\left[\frac{1}{r}\frac{\partial}{r}(ru_r) + \frac{1}{r}\frac{\partial u_\theta}{\partial\theta} + iku_z\right], \tag{10}$$

where $P_T = p + B_0b_z/\mu$ is the total (kinetic and magnetic) pressure perturbation, $C_S = \sqrt{\gamma p_0/\rho_0(r,\theta)}$ is the adiabatic sound speed and p_0 is the constant kinetic equilibrium plasma pressure. The above equations can be reduced to a system of equations given only in terms of the components of the velocity and total pressure perturbations, as

$$\frac{\rho_0}{\omega}\left(\omega^2 - k^2V_A^2\right)u_r = -i\frac{\partial P_T}{\partial r}, \tag{11}$$

$$\frac{\rho_0}{\omega}\left(\omega^2 - k^2V_A^2\right)u_\theta = -i\frac{1}{r}\frac{\partial P_T}{\partial\theta}, \tag{12}$$

$$\omega\rho_0 u_z = kP_T + i\frac{kB_0^2}{\mu r\omega}\frac{\partial}{\partial r}(ru_r) + i\frac{kB_0^2}{\mu r\omega}\frac{\partial u_\theta}{\partial\theta}. \tag{13}$$

In addition, from the definition of the total pressure perturbation, we have that

$$P_T = -i\rho_0\frac{C_S^2 + V_A^2}{\omega}\left[\frac{1}{r}\frac{\partial}{\partial r}(ru_r) + \frac{1}{r}\frac{\partial u_\theta}{\partial\theta}\right] + \rho_0\frac{kC_S^2}{\omega}u_z, \tag{14}$$

where $V_A(r,\theta) = B_0/\sqrt{\mu\rho_0(r,\theta)}$ is the Alfvén speed. Using the expressions that connect velocity components with the total pressure perturbation given by equations (11)–(14), we can derive a single equation for the total pressure perturbation as

$$\frac{\partial}{\partial r}\left[\frac{r}{\rho_0\left(\omega^2 - k^2V_A^2\right)}\frac{\partial P_T}{\partial r}\right] + \frac{1}{r}\frac{\partial}{\partial\theta}\left[\frac{1}{\rho_0\left(\omega^2 - k^2V_A^2\right)}\frac{\partial P_T}{\partial\theta}\right] - \frac{m_0^2 r}{\rho_0(\omega^2 - k^2v_A^2)}P_T = 0, \tag{15}$$

where the quantity m_0^2 is the magnetoacoustic parameter and it is defined as (Edwin & Roberts 1983)

$$m_0^2 = -\frac{\left(\omega^2 - k^2C_S^2\right)\left(\omega^2 - k^2V_A^2\right)}{\left(C_S^2 + V_A^2\right)\left(\omega^2 - k^2C_T^2\right)}, \tag{16}$$

with $C_T = C_SV_A/\sqrt{C_S^2 + V_A^2}$ being the tube speed. We should mention here, that although the form of m_0^2 agrees with its counterpart in homogeneous plasma, here all phase speeds are functions of r and θ.

In an inhomogeneous plasma with a density varying in the radial and azimuthal direction the system of equations describing the evolution of perturbations (see e.g. equations 11–13) is prone to the appearance of singularities that can lead to the appearance of resonances. The phenomenon of resonant absorption has been used extensively as a mechanism to explain plasma heating by waves, scattering of p-modes by sunspots, and damping of kink oscillations of coronal loops, etc. (Sakurai, Goossens & Hollweg 1991; Keppens, Bogdan & Goossens 1994; Ballai, Erdélyi & Goossens 2000; Ruderman & Roberts 2002). Indeed, equation (15) becomes singular at $\omega = \pm kV_A$. However, since we are dealing with waves in the short wavelength limit, where the propagation speed of slow body waves approaches the internal sound speed, the singularities will not appear.

In a homogeneous plasma, where ρ_0 is independent on r and θ, the total pressure perturbation has an azimuthal symmetry, i.e. proportional to $e^{im\theta}$, where m is the azimuthal wavenumber. As a consequence, the governing equation for the total pressure perturbation inside the cylinder simplifies to

$$\frac{\mathrm{d}^2P_T}{\mathrm{d}r^2} + \frac{1}{r}\frac{\mathrm{d}P_T}{\mathrm{d}r} - \left(m_0^2 + \frac{m^2}{r^2}\right)P_T = 0. \tag{17}$$

The sign of m_0^2 plays an important role, as for a combination of the characteristic speeds for which $m_0^2 > 0$, the flux tube supports the propagation of surface waves, i.e. waves that have their maximum amplitude at the boundary of the waveguide and show an evanescent behaviour inside the structure. For $m_0^2 = -n_0^2 < 0$, waves propagating along the flux tube will be body waves that have an oscillatory behaviour inside the flux tube and attain their minimum value at the boundary (Edwin & Roberts 1983).

According to the study by Edwin & Roberts (1983) the dispersion relation of MHD waves is obtained by matching the solutions obtained inside the magnetic flux tube (see equation 17) with the evanescent solutions obtained outside the flux tube. This matching implies the continuity of the total pressure and the radial component of the velocity perturbations at the boundary of the tube. The dispersion relations help in categorizing the possible waves propagating in a magnetic flux tube. Waves can oscillate such that the boundaries oscillate in phase (these modes are called the kink modes), but also waves for which the boundaries oscillate in anti-phase (also called sausage modes). Finally, cylindrical magnetic waveguides support the propagation of higher-order modes (called fluting modes) that disturb the symmetry axis of the waveguide in a more complicated way. Among all possible modes predicted by the theory developed by Edwin & Roberts (1983), the slow body modes analysed in our study are confined to the region between the tube speed, C_T, and the sound speed inside the tube, C_S. It is worth noting that the phase speed of slow body waves increases with increasing the wavenumber k or decreasing wavelength. In the thick flux tube approximation under photospheric conditions, the phase speed of slow body modes tends towards the internal sound speed, C_S.

Let us return to the inhomogeneous flux tube case. Since we are interested in body waves, from now on we will use n_0^2 as our magnetoacoustic parameter. In our analysis we will restrict ourselves to the thick flux tube limit, i.e. we consider that the wavelength of waves is much smaller than the radius of the tube ($kR \gg 1$). Furthermore, we assume that in this limit the behaviour of slow body modes is similar to the one in a homogeneous waveguide, therefore the phase speed of waves can be written as $\omega^2/k^2 \approx C_S^2(1-\nu)$, where ν is a small dimensionless positive quantity and $\nu = 1 - \omega^2/k^2C_S^2$.

Let us rewrite equation (15) for slow body modes into dimensionless form by introducing the new variable $\tilde{r} = r/R$. From now on, for simplicity, will drop the *tilde*. As a result, the dimensionless

governing equation for the total pressure perturbation (15) becomes

$$\frac{\partial}{\partial r}\left[\frac{r}{\rho_0(C_S^2-V_A^2)}\frac{\partial P_T}{\partial r}\right]+\frac{1}{r}\frac{\partial}{\partial \theta}\left[\frac{1}{\rho_0(C_S^2-V_A^2)}\frac{\partial P_T}{\partial \theta}\right]+\frac{n_0^2 r R^2}{\rho_0(C_S^2-V_A^2)}P_T=0. \tag{18}$$

By taking into account that the equilibrium plasma pressure is a constant quantity (in the presence of a homogeneous equilibrium magnetic field, this would correspond to the constant plasma-β limit), the coefficient function present in the terms of the above equation can be written as

$$\begin{aligned}\frac{1}{\rho_0(C_S^2-V_A^2)} &= \frac{1}{\rho_0\left(\gamma p_0/\rho_0 - B_0^2/\mu\rho_0\right)}\\ &= \frac{1}{\left(\gamma p_0 - B_0^2/\mu_0\right)}\\ &= \frac{1}{B_0^2/\mu_0}\frac{1}{(\gamma\beta/2-1)}.\end{aligned} \tag{19}$$

Here the plasma-β is constant and $V_A^2/C_S^2 = 2/\gamma\beta$. As a result, the governing equation for the total pressure perturbation becomes

$$\frac{\partial}{\partial r}\left(r\frac{\partial P_T}{\partial r}\right)+\frac{1}{r}\frac{\partial^2 P_T}{\partial \theta^2}-(kR)^2 \times\left(1-\frac{\omega^2}{k^2C_S^2(r,\theta)}\right)\left(1-\frac{2}{\gamma\beta}\right)rP_T=0. \tag{20}$$

The only term that contains information about the inhomogeneous character of the plasma is via the sound speed, $C_S(r,\theta)$, that appears in the third term of the above equation.

Before proceeding with our analysis we need to mention that our investigation is strictly applicable to slow body waves in the short wavelength limit, i.e. when the wavelength of waves is shorter than the radius of the circular waveguide. This limit is more likely to be applicable to larger sunspots and not to pores that can appear in different sizes. Indeed, the study by Gilchrist-Millar et al. (2021) showed that magnetoacoustic modes in small pores propagate with speeds of about 10 km s^{-1}, so the applicability of short wavelength in this case is questionable.

2.1 Transverse density profile

The inhomogeneous equilibrium plasma density distribution will be represented as a local density enhancement or depression of circular shape that depends on the variables r and θ in the form

$$\rho_0(r,\theta)=\rho_2\chi(r,\theta), \tag{21}$$

where $\chi(r,\theta)$ is the dimensionless quantity

$$\chi(r,\theta)=\left\{1+\frac{(\sigma-1)}{2}\left[1-\tanh\left(\frac{\psi(r,\theta)-\tau}{\xi}\right)\right]\right\}.$$

Here, $\sigma=\rho_1/\rho_2$ is the ratio of densities between the maximum value inside the inhomogeneous density region (ρ_1) and the homogeneous density in the annulus between the density enhancement/depletion and the circular waveguide (ρ_2). The function $\psi(r,\theta)$ is defined as

$$\psi(r,\theta)=\sqrt{(ar\cos(\theta)-\epsilon_1)^2+(br\sin(\theta)-\epsilon_2)^2},$$

where ϵ_1 and ϵ_2, describe the location of the centre of the density enhancement/depletion, τ is the ratio of the radii of the density inhomogeneity and the circular magnetic flux tube with $0<\tau<1$, ξ is the width of the annulus where the change of density occurs, i.e. gradual transition of density between two regions and a and b are

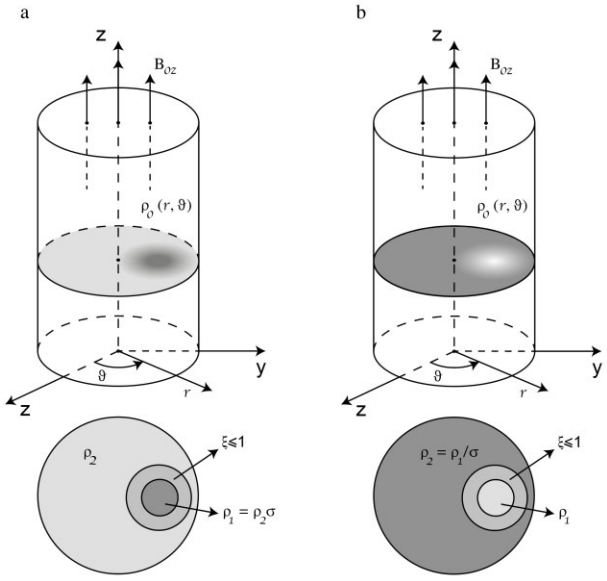

Figure 1. A schematic representation of the local equilibrium plasma density profile inhomogeneity inside the cylindrical waveguide in the case of a density enhancement (left column) and density depletion (right column). The top row shows the 3D configuration of density, while the bottom row represents a horizontal cut in the density distribution. The plots show (for illustration) an eccentric distribution of density with $\epsilon_1\neq0$ and $\epsilon_2=0$.

two quantities that describe the dimensionless length of the major and minor axis of an ellipse. The case $a=b=1$ corresponds to the circular density inhomogeneity and $a\neq b$ refers to a case where the density inhomogeneity has an elliptical shape. When $\epsilon_1=\epsilon_2=0$ we have a concentric density loading, while for any other pair of values, we have an eccentric case. Fig. 1 shows a representative distribution of the inhomogeneous equilibrium plasma density profile in the case of a density enhancement (panel a) and density depletion (panel b). The spatial structure of various slow body modes and the variation of the dimensionless eigenvalues for slow body modes, $V_{ph}=\omega/kC_S$ with respect to the parameters of the inhomogeneous equilibrium plasma density distribution will be studied numerically employing a suitable numerical algorithm for such a problem. The recovered dimensionless eigenvalues of our problem could also be interpreted as a quantitative measure of the change in the frequency. Given the particular equilibrium plasma model mentioned above, the inhomogeneous character of the plasma appears through the last term of equation (20), which can be written with the help of equation (21) as

$$\frac{\omega^2}{k^2C_S^2(r,\theta)}=\frac{\omega^2\rho_0(r,\theta)}{k^2\gamma p_0}=\frac{\omega^2\rho_2}{k^2\gamma p_0}\frac{\rho_0(r,\theta)}{\rho_2}=\frac{\omega^2}{k^2\tilde{C}_S^2}\chi, \tag{22}$$

where $\tilde{C}_S^2$ denotes the constant sound speed in the homogeneous annulus of density ρ_2. As before, for simplicity, will drop the *tilde* symbol. As a result, the governing equation for the total pressure becomes

$$\frac{\partial}{\partial r}\left(r\frac{\partial P_T}{\partial r}\right)+\frac{1}{r}\frac{\partial^2 P_T}{\partial \theta^2}-(kR)^2 \times\left(1-\frac{\omega^2}{k^2C_S^2}\chi\right)\left(1-\frac{2}{\gamma\beta}\right)rP_T=0. \tag{23}$$

The quantity $\omega/kC_S=V_{ph}$ is the dimensionless phase speed of waves. The above equation is a Sturm–Liouville eigenvalue equation and the

Table 1. Values of the physical parameters used for the numerical modelling and analysis. Unless specified otherwise, for each case we consider $kR = 4$ and $\beta = 3 \times 10^{-3}$.

	σ	τ	ξ	ϵ_1	ϵ_2
C1: Uniform density	1				
C2: Non-uniform density enhancement					
C2.1: – concentric	2.5	0.3	9.1×10^{-2}	0	0
C2.2: – right eccentric	2.5	0.3	9.1×10^{-2}	0.25	0
C2.3: – upper right eccentric	2.5	0,3	9.1×10^{-2}	0.25	0.25
C3: Non-uniform density depletion					
C3.1: – concentric	0.5	0.7	9.1×10^{-2}	0	0
C3.2: – right eccentric	0.5	0.7	9.1×10^{-2}	0.25	0
C3.3: – upper right eccentric	0.5	0.7	9.1×10^{-2}	0.25	0.25
C4: Variation of V_{ph}					
C4.1: $2 \leq kR \leq 10$	2.5; 0.5	0.3; 0.7	9.1×10^{-2}	0; 0.35	0; 0.35
C4.2: $3 \times 10^{-6} \leq \beta \leq 3 \times 10^{-3}$	2.5; 0.5	0.3; 0.7	9.1×10^{-2}	0; 0.35	0; 0.35
C4.3.1: $2 \leq \sigma \leq 10$		0.3; 0.7	9.1×10^{-2}	0; 0.35	0; 0.35
C4.3.2: $0.45 \leq \sigma \leq 0.9$		0.3; 0.7	9.1×10^{-2}	0; 0.35	0; 0.35
C4.4: $0.3 \leq \tau \leq 0.7$	2.5; 0.5		9.1×10^{-2}	0; 0.35	0; 0.35
C4.5: $1.8 \times 10^{-5} \leq \xi \leq 0.1$	2.5; 0.5	0.3; 0.7		0; 0.35	0; 0.35
C4.6: $0.1 \leq \epsilon_1 \leq 0.5$	2.5; 0.5	0.3; 0.7	9.1×10^{-2}		0; 0.35

eigenvalues as well as the corresponding eigenfunctions can be determined using a numerical approach for particular inhomogeneous density distribution assuming that $P_T(r, \theta) = 0$ at the boundary of the tube corresponding to $r = 1$.

3 DESCRIPTION OF THE NUMERICAL METHOD

Given the particulars of the problem, the most suitable method to deal with such an equation is the FCS collocation method over the Dirichlet boundary condition $P_T(r = 1, \theta) = 0$. Spectral collocation methods appear to offer the greatest accuracy for the least computational expense for this class of problems. In order to implement the numerical algorithm, equation (23) can be written as

$$\frac{\partial}{\partial r}\left(r\frac{\partial P_T}{\partial r}\right) + \frac{1}{r}\frac{\partial^2 P_T}{\partial \theta^2} + \kappa_0^2 r P_T - \kappa_0^2 \chi V_{ph}^2 r P_T = 0, \tag{24}$$

where $\kappa_0^2 = -(kR)^2(1 - 2/\gamma\beta)$. To implement the FCS and obtain the eigenvalues and the corresponding eigenfunctions of equation (24), we will write this equation in a compact form as

$$\left(\frac{\partial^2}{\partial r^2} + \frac{1}{r}\frac{\partial}{\partial r} + \frac{1}{r^2}\frac{\partial^2}{\partial \theta^2} + \kappa_0^2 - \kappa_0^2 \chi V_{ph}^2\right) P_T = 0. \tag{25}$$

Our numerical model is smoothly non-uniform allows a gradual decrease in density of the loaded regions and avoids abrupt change in density. To capture the rapid variation in density, a larger number of grid points are required for the non-uniform cross-sectional configurations of magnetic flux tube, particularly in the radial direction. Details on the numerical solution of the above governing equation are provided in the Appendix.

4 RESULTS

In this section, we will analyse the dependence of the phase speed of slow body modes and the spatial structure of the total pressure perturbation on the magnetic flux tube density inhomogeneity under solar photospheric conditions.

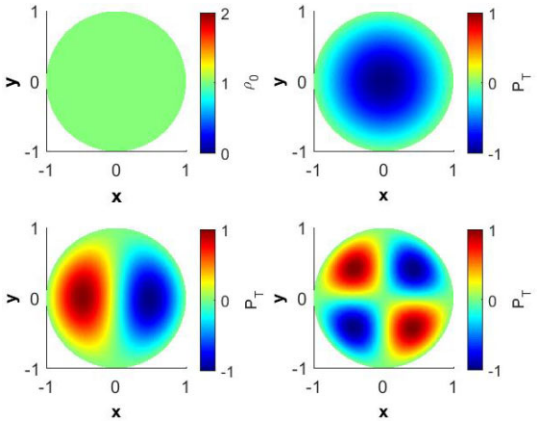

Figure 2. The density distribution (upper left panel) and the spatial structure of SSFB, SKFB, and SF2FB modes under photospheric conditions in a circular magnetic flux tube with uniform density ($\sigma = 1$). The colour bars display the magnitude of the total pressure perturbation amplitude divided by its maximum value. The red and blue shaded regions represent crests (maxima) and valleys (minima) of amplitude variation of total pressure perturbation.

4.1 The spatial structure of slow body modes in the presence of a uniform density

The propagation of the MHD waves in a homogeneous cylindrical waveguide with uniform equilibrium density corresponds to case C1 (see Table 1), i.e. to the particular value of $\sigma = 1$ in equation (21) and previously this scenario was studied in detail by Edwin & Roberts (1983). Fig. 2 shows the homogeneous distribution of normalized equilibrium density (left upper panel) and the spatial structure of the total pressure perturbation in the case of slow sausage fundamental body (SSFB, right upper panel), slow kink fundamental body (SKFB, left lower panel) and slow fluting fundamental body mode of order 2 (SF2FB, right lower panel). These results clearly show that in the homogeneous limit, slow body modes of different azimuthal order have global harmonic character. The colour bar displays the magnitude of the dimensionless amplitude of the total pressure perturbation, P_T, with the red and blue shaded regions representing crests (maxima) and valleys (minima) of the amplitude.

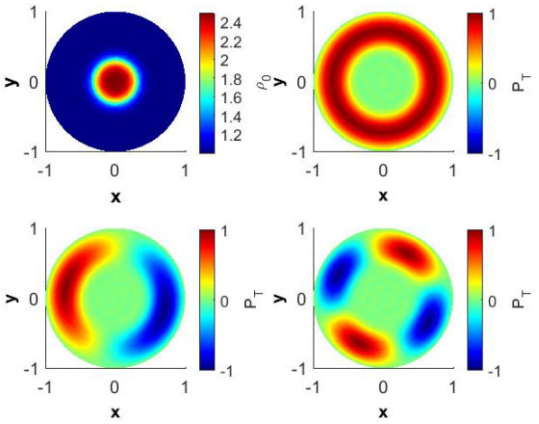

Figure 3. The same modes as in Fig. 2, but here we show the results in the presence of a concentric density enhancement. All characteristic values of parameters used in these numerical solutions correspond to the case C2.1 in Table (1).

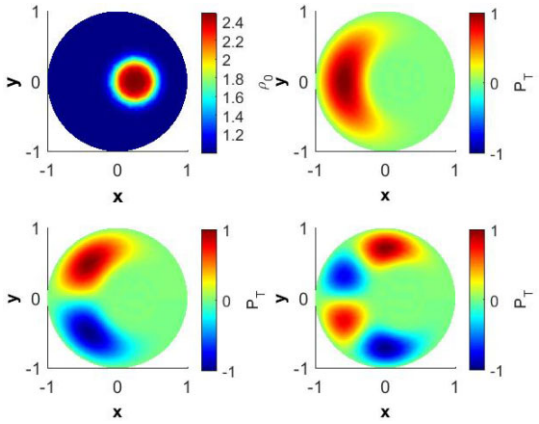

Figure 4. The same MHD modes as in Fig. 3, but here we show the results for an eccentric density loading, situated along the horizontal direction. The parameters used for this visualization are given as case C2.2 in Table 1.

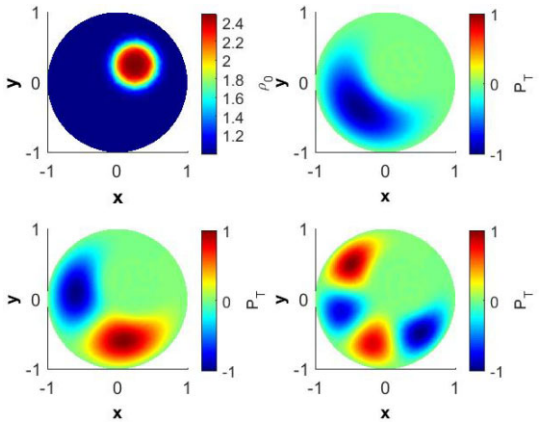

Figure 5. The same MHD modes as in Fig. 3, but here we show the results for an eccentric density loading, situated along the first bisector. The parameters used for this visualization are given as case C2.3 in Table 1.

4.2 The spatial structure of slow body modes in the presence of a non-uniform density

The changes in the spatial structure of slow body waves as well as the modification of the dimensionless phase speed in terms of the parameters of local equilibrium plasma density given by equation (21) will be discussed when the inhomogeneous density is represented as a local density enhancement ($\sigma > 1$) and density depletion ($\sigma < 1$). The modifications in the oscillatory patterns of waves are analysed for three particular positions of the equilibrium density loading, e.g. concentric (case C2.1), right eccentric (case C2.2), and upper right eccentric (case C2.3). The description of parameters related to these three cases is described in Table 1.

4.2.1 Slow body modes in the presence of concentric and eccentric density enhancements

Due to the changes in the values of the radial distribution of equilibrium density, it is expected that the dimensionless phase speed and the spatial structure of slow body waves will be modified. Let us first discuss the case C2.1. Fig. 3 shows the radial distribution of the equilibrium density and the spatial distribution of the normalized value of the total pressure perturbation of SSFB, SKFB, and SF2FB modes. In the presence of concentric inhomogeneity the corresponding eigenmodes migrate towards the boundary of the waveguide, i.e. in the direction of lower density. By comparing Figs 2 and 3 it is evident that obtained MHD modes become more localized but, at the same time, maintain their symmetry with respect to the centre of the flux tube. The regions where no oscillations are possible correspond to the combination of physical parameters that will make the value of n_0^2 in equation (18) change sign, so the governing equation does not describe the eigenfunction of a body mode. Surface waves cannot be cast in our description, as we had to impose a Dirichlet-type boundary condition, that cannot be applied to surface waves. These regions simply show that here we have no slow body modes.

The enhanced eccentric equilibrium density distribution corresponds to a density loading whose position is shifted away from the origin (case C2.2) and the position of its centre is controlled by the two parameters, ϵ_1 and ϵ_2. In reality, the position of the inhomogeneous density loading can be arbitrary, however, in this study we discuss only cases that correspond to the shifted inhomogeneous density along the horizontal axis (Fig. 4, parameters given by case C2.2), and a position where both quantities describing the location of the density load are non-zero (Fig. 5, parameters given by case C2.3 in Table 1).

Fig. 4 shows the radial distribution of the equilibrium density and the spatial structure of the normalized total pressure perturbation for the same slow body modes as before. Due to the considered density loading, the spatial extent of the eigenfunction shrinks and the global nature of these modes ceases. Comparing Figs 2 and 4, it is evident that the oscillations are shifted, again, towards regions of lower density, so they become more localized. When the density inhomogeneity is shifted along an arbitrary direction (along the first bisector as in Fig. 5, the modification in the spatial structure of modes remains qualitatively the same.

4.2.2 Slow body modes in the presence of concentric and eccentric equilibrium density depletions

In the case of a depleted density inhomogeneity, the maximum value of density of the inhomogeneous region is less than the density of the homogeneous part of the waveguide, i.e. $\sigma < 1$. The values of parameters used for our numerical investigations are given in Table 1 (case C3). Fig. 6 (case C3.1) shows the spatial structure of the normalized total pressure perturbation corresponding to the same

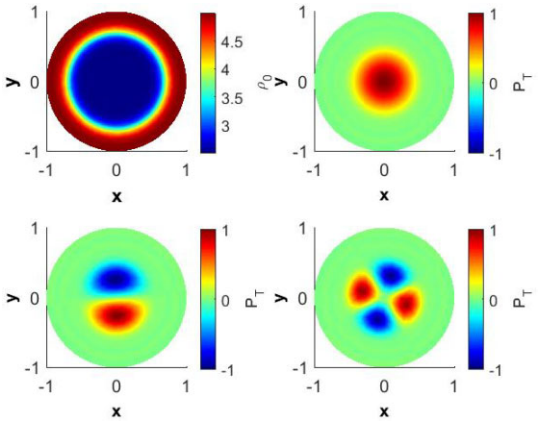

Figure 6. The same as in Fig. 3 but for the case of depleted concentric equilibrium density inhomogeneity. The parameters used for this visualization are given as case C3.1 in Table 1.

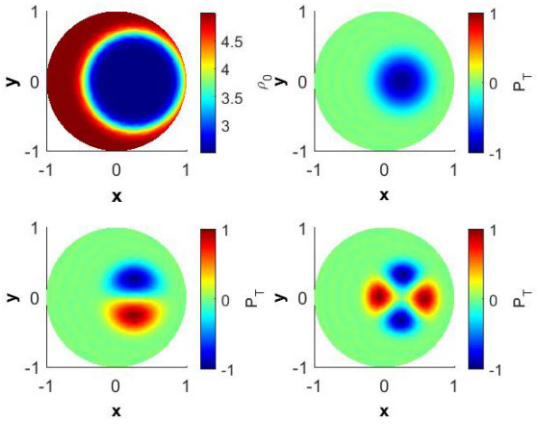

Figure 7. The same as in Fig. 6, but here the depleted density region is situated in an eccentric position along the horizontal axis. The parameters used for this visualization are given as case 3.2 in Table 1.

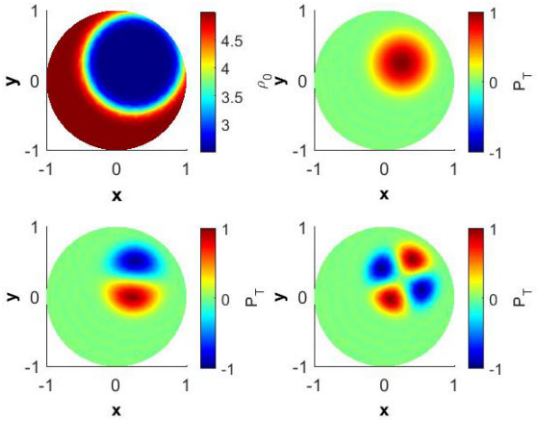

Figure 8. The same as in Fig. 6 but here the depleted density inhomogeneity is placed along the first bisector. The parameters used for this visualization are given as case 3.3 in Table 1.

body modes as before in the case of concentric loading, while Figs 7 (case C3.2) and 8 (case C3.3) show the spatial structure of the total pressure for an eccentric loading, when the density inhomogeneity is placed along the horizontal axis and in a position along the first bisector.

The results obtained for this case confirm the previous findings, namely that in the case of an inhomogeneous distribution of the equilibrium plasma density, the modes tend to lose their global character, instead they become localized in the region that corresponds to the lowest density. However, in contrast to the case C2 of density enhancement, in this case, the modes tend to be attached to the region of equilibrium density inhomogeneity. Moreover, unlike the distorted shape of modes found in case C2, the slow body modes in the depleted density case maintain their symmetric character. As before, the spatial structure of slow body modes does not change if the density loading is placed along the horizontal or vertical axes.

The migration of the location of modes in the presence of density inhomogeneity obtained for the density enhancement and depletion reveals one important consequence for observations. A localized wave observation in a sunspot could be a way to identify the location of a density inhomogeneity in the umbral region, even if this inhomogeneity cannot be seen in observations.

4.3 Comparative study of the variation of the phase speed of slow body modes in the presence of an inhomogeneous density distribution

The results presented in the previous section show that the spatial structure of slow body modes propagating in a circular waveguide is influenced by a density inhomogeneity by the modifications in the location of these modes. However, due to the modification in the azimuthal symmetry, it is natural to expect that these modes are affected by changes in the phase speed of waves or their frequency. To address this problem in this section we carry out a comparative study of the variation of the dimensionless phase speed of body waves (or their dimensionless frequency) in terms of the parameters related to the plasma environment in which these waves propagate and wave characteristics (dimensionless wavenumber, kR, plasma-β), but also in terms of the parameters describing the inhomogeneous density (σ, τ, ξ and the values of the ϵ parameters). The details of the parameters used are summarized in Table 1 (case C4). The first two parameters (kR and β) are parameters that influence the solution through equation (23). The study will be performed considering the homogeneous density case as a benchmark value.

As the mathematical model described earlier refers to the short wavelength limit (wide flux tube), first we investigate the variation of the dimensionless phase speed of waves with the dimensionless wavenumber of body waves (for a constant tube radius the variation of the kR parameter is, in fact, describing the variation of the wavenumber, with increasing kR corresponding to a decrease in the wavelength of waves). Fig. 9 (left panel) shows the variation of dimensionless phase speed for the three slow body modes with respect to kR in the case of uniform density: SSFB (solid line), SKFB (dash line) and SF2FB (dotted line). The three waves show a distinctive dispersive character for lower values of kR, while their dimensionless phase speed becomes practically independent of the wavelength of waves for higher values of kR, the dimensional speed of each wave tending to the sound speed, C_S. Since waves propagate faster for smaller wavelengths, these waves are known to have a positive dispersion. The behaviour of modes obtained here is similar to the variation of the phase speed determined by Edwin & Roberts (1983). This result also proves our initial assumption according to which the Dirichlet boundary condition imposed in our case would not modify qualitatively or quantitatively the solution of dispersion relation obtained in the case of body modes (in line with the recent

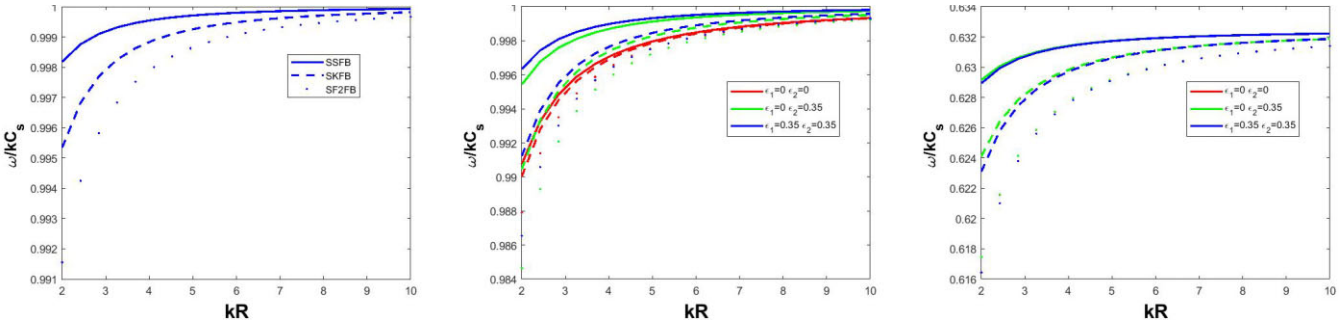

Figure 9. The variation of the dimensionless phase speed of slow body waves with the dimensionless wavenumber kR for a uniform loading with $\sigma = 1$ (left panel) for the three slow body modes (SSFB, solid blue curve), SKFB (dashed blue curve), SF2FB (dotted blue curve. Middle panel: the variation of the same quantity in the case of an inhomogeneous density enhancement at three different positions (shown in the legend). Right panel: the variation of the same quantity for a depleted density inhomogeneity for the same three positions. The values of parameters used in these plots are given as case 4.1 in Table 1.

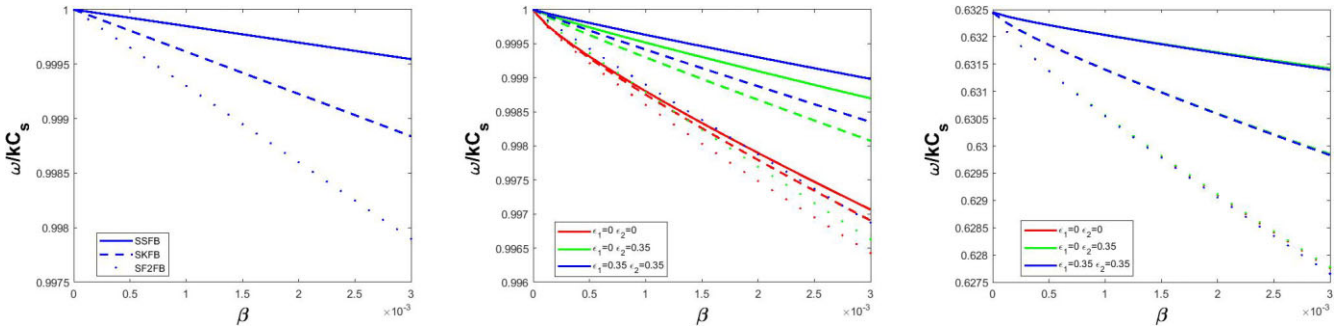

Figure 10. The same as in Fig. 9, but here we investigate the variation of the dimensionless phase speed with respect to plasma-β. The values of parameters used in these plots are given as case 4.2 in Table 1.

findings by Aldhafeeri et al. (2022)). For a particular wavenumber, it is clear that the fluting mode is the most sensitive to the variation in size of the waveguide, confirming the results by Albidah et al. (2022).

The middle and right panels of Fig. 9 show the variation of dimensionless phase speed for the same slow body modes with respect to kR in the case of density enhancement and depletion, respectively. The three positions of the density inhomogeneity are shown by different colours: concentric (red) and two eccentric cases (green and blue). Similar to the case of uniform plasma, in the enhanced and depleted density distribution we observe the same dispersive character for smaller values of kR and the dimensionless phase speed becoming practically independent on the wavelength of waves for the higher values of kR. Comparing the values of the dimensionless phase speed in the three cases, it is evident that the density enhancement leaves practically the dimensionless phase speed unchanged, while the density depletion brings a more significant reduction in the dimensionless phase speed (of nearly 40 per cent) compared to the homogeneous case. In the case of density enhancement, the concentric distribution of density leads to a much more differentiated behaviour of the dimensionless phase speed, especially in the case of sausage modes. Interestingly, in the depleted density distribution the modes show a larger variation with respect to the position of the density inhomogeneity, however, the distinction of waves' phase speed with regards to the position of the inhomogeneity vanishes. These plots show that once a density inhomogeneity is taken into account, the phase speeds of particular waves become much closer, making them rather difficult to distinguish from one another.

Another important parameter that plays a crucial role in the propagating characteristic of waves is the plasma-β. In the solar photosphere the intensive magnetic field in sunspots or pores makes this parameter very small. Eq (23) confirms that the eigenvalues determined for the studied slow waves will also depend on the plasma-β. Fig. 10 (left panel) shows the variation of the slow waves' dimensionless phase speed with the plasma-β parameter for a homogeneous density ($\sigma = 1$). Clearly, for very low plasma β, the value of ω/kC_S is approximately 1 for all three eigenmodes and corresponds to the value of the phase speed in an unbounded plasma. With the increase of plasma-β, the value of ω/kC_S decreases fairly linearly for all the three eigenmodes, however, these changes are rather small and the most affected mode is the fluting mode of order 2. The middle and right panels of Fig. 10 show the variation of phase speed for the same slow body modes with respect to the same parameter in the case of density enhancement ($\sigma > 1$) and depletion ($\sigma < 1$). The locations of density inhomogeneity (and the colours used to represent these) are identical to the ones used in Fig. 9. Similar to the case of uniform plasma, the variation of the dimensionless phase speed shows the same decreasing pattern with the increase of plasma-β. Similar to the results shown in Fig. 9 the density enhancement does not lead to significant changes in the variation of the phase speed, while these changes are more significant in the case of depleted density inhomogeneity. While in the case of density enhancement, there is a clear dependence of the phase speed in terms of the location of the inhomogeneity (the concentric case showing the lowest values), the differentiation of the same mode for the three different locations ceases, practically they are independent on the location of the density inhomogeneity.

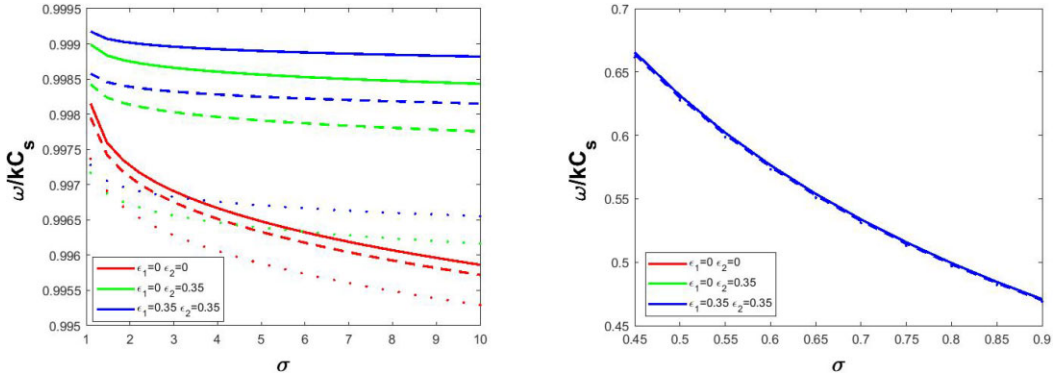

Figure 11. The same as in Fig. 9, but here we show the variation of the dimensionless phase speed with respect to the parameter σ in the case of a density enhancement (left panel) and density depletion (right panel). The values of parameters used in these plots are given as case C4.3.1 (left panel) and case C4.3.2 (right panel) in Table 1.

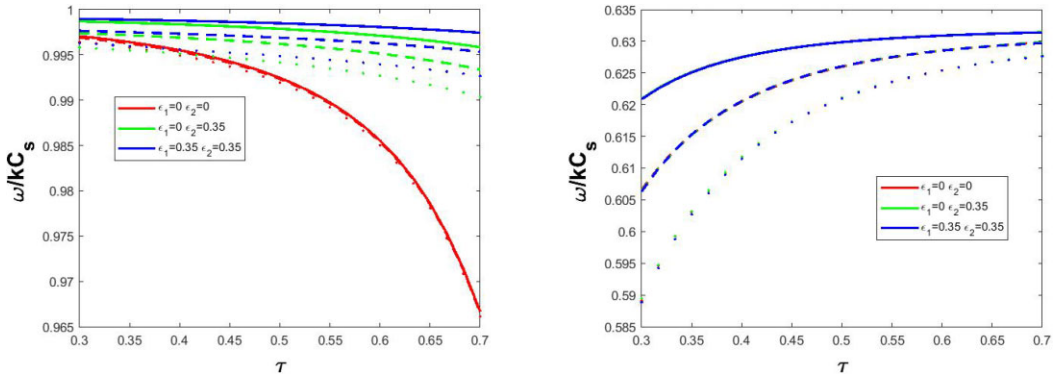

Figure 12. The same as in Fig. 9, but here we plot the variation of the dimensionless phase speed of different slow body waves in terms of the parameter τ in the case of density enhancement (left panel) and depletion (right panel). The values of parameters used in these plots are given as case C4.4 in Table 1.

Let us now discuss the variation of the dimensionless phase speed of slow waves of different azimuthal order in terms of the parameters describing the density inhomogeneity (cases C4.3.1–C4.6 in Table 1). Fig. 11 (left panel) shows the variation of ω/kC_S for the three slow body modes in terms of the parameter σ in the case of a density enhancement, with the value of $\sigma = 1$ corresponding to the homogeneous density. As before, the different line styles and colours show different slow body modes and three different positions of density inhomogeneity. With the increase in the value of σ the dimensionless phase speed decreases for all three eigenmodes. This decrease is more pronounced near $\sigma = 1$ and becomes fairly linear for larger values of σ. From the figure (and all subsequent cases discussed in this study) it is obvious that the fundamental slow sausage mode has the highest propagation speed. For a particular value of σ the differences in the propagation speed of these three waves are very small. The largest modification in the phase speed of waves occurs in the case of concentric loading, and the changes of this quantity with the strength of inhomogeneity for any eccentric position have little variation.

Fig. 11 (right panel) shows the variation of ω/kC_S of slow body modes for a depleted density loading with respect to σ. In contrast to the case of an enhanced density, the dimensionless phase speed of the investigated slow waves shows a much stronger dependence on the value of the density inhomogeneity, however, waves propagate with the same phase speed, regardless of the position of the density depletion, meaning that observationally it would be impossible to distinguish between these waves if we restrict our mode identification based on the propagation speed. The propagation speeds of waves in this case are also independent of the type of waves, all body waves (regardless of their radial order) tend to propagate with the same phase speed.

The variation of the dimensionless phase speed of selected slow body modes with respect to the parameter τ (case C4.4 in Table 1), denoting the ratio of the radii of the density inhomogeneity to the radius of the tube, in the case of a density enhancement and depletion, is shown in the two panels of Fig. 12. The meaning of different line styles and colours is identical to previous cases. In the case of density enhancement, with the increase in the size of the inhomogeneity, the dimensionless phase speeds decrease very little for eccentric density loading, while the variation of the phase speed in the case of concentric loading shows the most accentuated variation, however, the distinction of the type of waves ceases. These conclusions are similar to the findings on the variation of the modes' phase speed with the parameter σ.

Fig. 12 (right panel) shows the variation of ω/kC_S for the same three slow body modes with respect to the parameter τ when the density inhomogeneity takes a depleted value (see case C4.4 in Table 1). With the increase of the size of the inhomogeneous region, the value

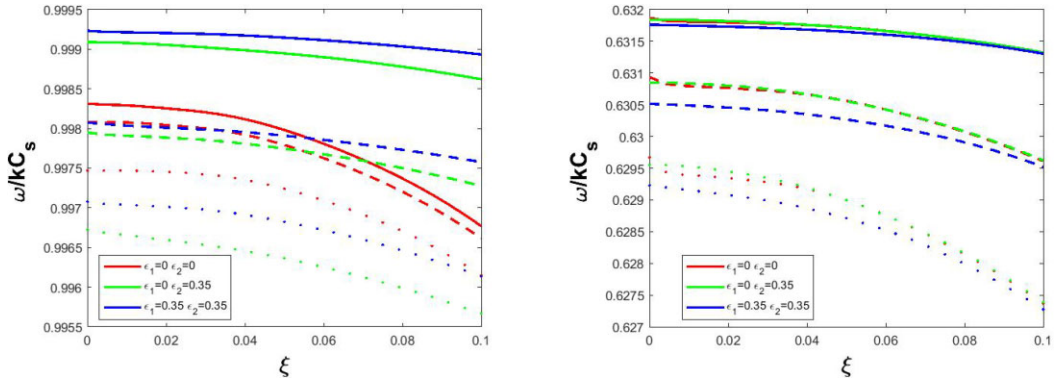

Figure 13. The same as in Fig. 9, but here we display the variation of the dimensionless phase speed of slow body waves in terms of the smoothness parameter, ξ (see case C4.5 in Table 1), in the case of an equilibrium density enhancement (left panel) and depletion (right panel). The values of parameters used in these plots are given as case C4.5 in Table 1.

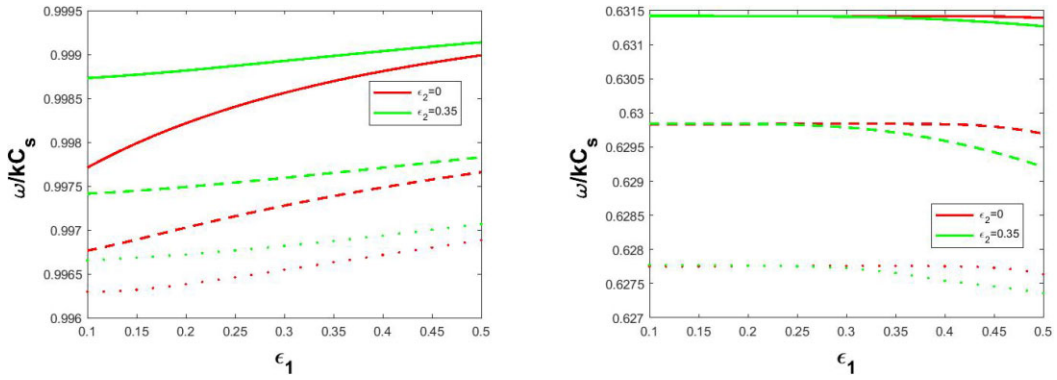

Figure 14. The variation of the dimensionless phase speed of slow body waves in terms of the parameter ϵ_1 for two particular values of ϵ_2. The cases of density enhancement and depletion are shown in the right and left panels, respectively. The values of parameters used in these plots are given as case C4.6 in Table 1.

of ω/kC_S increases, and the variation of the dimensionless phase speed is practically independent of the location of the inhomogeneity. This result has interesting implications, as the location of the inhomogeneous region can be chosen, for modelling purposes, in a position that is most suitable for modelling. In the depleted density case the fundamental sausage mode displays the smallest variation with the ratio of radia, τ. Comparing the two panels of Fig. 12 it is obvious that the phase speeds corresponding to a depleted case show a much enhanced variation with τ.

The variation of the dimensionless phase speed of the investigated slow body waves with respect to the smoothness parameter, ξ (see case C4.5 in Table 1), is shown in Fig. 13 for an inhomogeneous equilibrium density enhancement (left panel) and density depletion (right panel), respectively. In the case of a density enhancement the values of the phase speed decrease for all three modes with the increase in the value of ξ. This decrease is fairly linear except for sausage modes for concentric loading. As before, for a particular value of ξ, the sausage mode has the highest propagation speed. The phase speed of waves for a concentric density distribution shows the largest variability. On the other hand, in the case of depleted density, the phase speed of waves is much reduced compared to the case of density enhancement and the variation of the dimensionless phase speed for the three modes shows a great degree of independence on the location of the inhomogeneity. The most affected mode remains the fluting and sausage modes. They are practically independent of the change of the smoothness parameter in the case of depleted density.

Finally, in Fig. 14 we investigate the variation of the dimensionless phase speed for the three investigated slow body modes in terms of the position of the centre of the density inhomogeneity. For this parametric analysis, we let the value of the parameter ϵ_1 (see case C4.6 in Table 1) vary in a given interval and choose two particular values of ϵ_2: $\epsilon_2 = 0$ (red curves) and $\epsilon_2 = 0.35$ (green curves). The two panels of Fig. 14 represent the cases of density enhancement, respectively. With the increase in the value of the parameter ϵ_1, the dimensionless phase speed of investigated slow body modes corresponding to a density enhancement increases with the departure from the concentric case, but the difference between the phase speed corresponding to the two particular values of ϵ_2 diminishes with the increase of ϵ_1. It is also clear that the increase with ϵ_1 is nearly linear when the density inhomogeneity is not along the horizontal axis. For a given value of ϵ_1, the fundamental sausage modes have the highest propagation speed. In the case of depleted density, the dimensionless phase speed of slow body waves shows practically no (or little) variation with the location of the density inhomogeneity, meaning that when modelling the effect of density inhomogeneity on the propagation characteristics of waves we can choose the most convenient location.

5 CONCLUSIONS

Intense magnetic waveguides in the solar photosphere, such as pores and sunspots, are ideal environments for the propagation of guided waves. The theory developed by Edwin & Roberts (1983) predicts the qualitative behaviour of different waves in such environments assuming an ideal case when the plasma is homogeneous, without background flows, and unbounded along the symmetry axis of the magnetic flux tube. High-resolution observations show that these restrictions are not realistic and the theory of guided MHD waves must be expanded to account for the presence of density inhomogeneity.

Observations show that sunspots and pores are inhomogeneous both in magnetic field and density. These inhomogeneities can alter the frequency of waves and their propagation speed leading to a real challenge to identify the nature of waves and their properties. This study investigates the modification of the properties of waves (their spatial structure, phase speed or frequency, in particular) in the presence of a symmetric and geometrically well-defined inhomogeneity.

In order to tackle the problem mathematically we employed results previously obtained by Aldhafeeri et al. (2022), who showed that in the case of slow body waves under photospheric conditions the dispersive character of waves and their properties can be confidently described by solving a Helmholtz equation with Dirichlet boundary condition. In addition, we assumed a situation when the wavelength of waves is much smaller than the radius of the tube (short wavelength limit). The eigenfrequency as well as the eigenfunction of waves was studied as a Sturm–Liouville eigenvalue problem and the governing equation with non-constant coefficients was solved numerically using the FCS method.

The inhomogeneous equilibrium plasma density considered here was described by a series of parameters with the aim of highlighting what effects these parameters have on the characteristics of waves. In order to provide a general approach, we have considered both cases of an enhanced and depleted equilibrium plasma density.

Since our model assumed a photospheric waveguide where the equilibrium plasma pressure is constant, these equilibrium density enhancements and depletions would appear as cooler (darker) and hotter (brighter) regions inside a magnetic waveguide. The advantage of the density profile given by equation (21) is its versatility for modelling purposes. The large number of parameters used to describe the strength, size, location, etc., of the equilibrium density helps to describe realistic situations.

First of all, we conclude that a significant change driven by the inhomogeneous equilibrium plasma density is the modification in the spatial structure of waves. A direct consequence of the particular density distribution is that slow body waves in cylindrical waveguides lose their global character, instead, they become more localized and always tend to appear in the regions that correspond to a lower density. This property might help identify locations of density inhomogeneity when these are not visible in intensity spectral lines.

The parameters that describe the equilibrium plasma density modification (strength, location, size, smoothness of the transition to a homogeneous density) affect the modes in different ways. In general, the eigenfrequencies of fluting modes are more sensitive to the modifications of the equilibrium plasma density parameters. In the case of depleted density, the modifications in the phase speed of waves are more important (nearly 40 per cent decrease) and the differentiation between different modes according to the size of the inhomogeneity or its location very often is very small, meaning that for modelling purposes one can choose the most convenient location for equilibrium plasma density inhomogeneity.

The analysis and the numerical recipe in this study can be considered as a starting point in the investigation of waves in realistic solar photospheric waveguides, where the equilibrium plasma density inhomogeneity derived from observations or realistic sunspot simulations can be incorporated in the study of the properties of slow body waves. This analysis can be considered as a tool for diagnostic of the inhomogeneous character of sunspots or pores; however, this diagnostics is rather qualitative, rather than quantitative. The choice of a waveguide of high symmetry is not entirely realistic; however, it allows us to use a fairly simple mathematical approach and the obtained results show the modifications of the properties of waves due solely to the density inhomogeneity. It is known (see e.g. Albidah et al. 2021, 2022) that the irregular shape of the waveguides has very serious effects on the spatial structure of waves, especially in the case of higher order modes. The constant plasma-β limit considered here is also a rather crude approximation. Observations show (see e.g. Gary 2001; Grant et al. 2018) that the plasma beta changes over small spatial scales, and around the density inhomogeneities the plasma beta may exhibit a sharp gradient. Finally, a more realistic model, involving inhomogeneous magnetic field and temperature, will be developed and studied in the near future.

ACKNOWLEDGEMENTS

FA is grateful to Taibah University's Deanship of Scientific Research (DSR) for enabling him to pursue his PhD studies at The University of Sheffield. VF and GV are grateful to the Science and Technology Facilities Council (STFC) grant ST/V000977/1. VF, GV, and IB thank the Institute for Space-Earth Environmental Research (ISEE, International Joint Research Program, Nagoya University, Japan); Royal Society, International Exchanges Scheme, collaboration with Chile (IE170301), Brazil (IES/R1/191114), Greece (IES/R1/221095), Australia (IES/R3/213012), and India (IES/R1/211123) for the support provided. This research has also received financial support from the European Union's Horizon 2020 research and innovation program under grant agreement No. 824 135 (SOLARNET).

DATA AVAILABILITY

The data underlying this article will be shared on reasonable request to the corresponding author(s).

REFERENCES

Albidah A., Brevis W., Fedun V., Ballai I., Jess D., Stangalini M., Higham J., Verth G., 2021, Phil. Trans. R. Soc. A, 379, 20200181
Albidah A. B. et al., 2022, ApJ, 927, 201
Aldhafeeri A. A., Verth G., Brevis W., Jess D. B., McMurdo M., Fedun V., 2021, ApJ, 912, 50
Aldhafeeri A. A., Verth G., Fedun V., Lennard M., Ballai I., 2022, ApJ, 938, 32
Ballai I., 2007, Sol. Phys., 246, 177
Ballai I., Erdélyi R., Goossens M., 2000, J. Plasma Phys., 64, 235
Ballester J. L., 2005, Space Sci. Rev., 121, 105
Banerjee D. et al., 2021, Space Sci. Rev., 217, 76
Beckers J. M., Schultz R. B., 1972, Sol. Phys., 27, 61
Beckers J. M., Tallant P. E., 1969, Sol. Phys., 7, 351
De Moortel I., Browning P., 2015, Phil. Trans. Soc. A, 373, 20140269
De Moortel I., Nakariakov V. M., 2012, Phil. Trans. Soc. A, 370, 3193
De Pontieu B. et al., 2007, Science, 318, 1574
Edwin P. M., Roberts B., 1983, Sol. Phys., 88, 179

Erdélyi R., Ballai I., 2007, Astron. Nachr., 328, 726
Feng S., Zhao Y., Yang Y., Ji K., Deng H., Wang F., 2015, Sol. Phys., 290, 1119
Forgács-Dajka E., Dobos L., Ballai I., 2021, A&A, 653, A50
Garcia de La Rosa J. I., 1987, Sol. Phys., 112, 49
Gary G. A., 2001, Sol. Phys., 203, 71
Gilchrist-Millar C. A. et al., 2021, Phil. Trans. R. Soc. A, 379, 20200172
Grant S. D. T. et al., 2015, ApJ, 806, 132
Grant S. D. T. et al., 2018, Nat. Phys., 14, 480
Grant S. et al., 2022, ApJ, 938, 143
Henriques V. M. J., Nelson C. J., Rouppe van der Voort L. H. M., Mathioudakis M., 2020, A&A, 642, A215
Jess D. B., De Moortel I., Mathioudakis M., Christian D. J., Reardon K. P., Keys P. H., Keenan F. P., 2012, ApJ, 757, 160
Jess D. B., Morton R. J., Verth G., Fedun V., Grant S. D. T., Giagkiozis I., 2015, Space Sci. Rev., 190, 103
Jess D. B., Jafarzadeh S., Keys P. H., Stangalini M., Verth G., Grant S. D. T., 2023, Living Rev. Sol. Phys., 20, 1
Ji K., Jiang X., Feng S., Yang Y., Deng H., Wang F., 2016, Sol. Phys., 291, 357
Keppens R., Bogdan T. J., Goossens M., 1994, ApJ, 436, 372
Keys P. H. et al., 2018, ApJ, 857, 28
Khomenko E., Collados M., 2015, Living Rev. Sol. Phys., 12, 6
Kilcik A., Sarp V., Yurchyshyn V., Rozelot J.-P., Ozguc A., 2020, Sol. Phys., 295, 58
Li B., Antolin P., Guo M. Z., Kuznetsov A. A., Pascoe D. J., Van Doorsselaere T., Vasheghani Farahani S., 2020, Space Sci. Rev., 216, 136
Li K., Li J., Lu X., Chen S., 2022, Contrib. Plasma Phys., 62, e202100056
Louis R. E., Mathew S. K., Bellot Rubio L. R., Ichimoto K., Ravindra B., Raja Bayanna A., 2012, ApJ, 752, 109
Mathioudakis M., Jess D. B., Erdélyi R., 2013, Space Sci. Rev., 175, 1
Morton R. J., Erdélyi R., Jess D. B., Mathioudakis M., 2011, ApJ, 729, L18
Nakariakov V. M., Ofman L., Deluca E. E., Roberts B., Davila J. M., 1999, Science, 285, 862
Oliver R., 2009, Space Sci. Rev., 149, 175
Riethmüller T. L., Solanki S. K., Zakharov V., Gandorfer A., 2008, A&A, 492, 233
Rimmele T., 2008, ApJ, 672, 684
Ruderman M. S., Roberts B., 2002, ApJ, 577, 475
Sakurai T., Goossens M., Hollweg J. V., 1991, Sol. Phys., 133, 227
Sathej G., Adhikari R., 2009, Acoust. Soc. Am. J., 125, 831
Schüssler M., Vögler A., 2006, ApJ, 641, L73
Sekii T. et al., 2007, PASJ, 59, S637
Skirvin S. J., Fedun V., Silva S. S. A., Verth G., 2022, MNRAS, 510, 2689
Solanki S. K., 2003, A&AR, 11, 153
Stangalini M., Del Moro D., Berrilli F., Jefferies S. M., 2011, A&A, 534, A65
Stangalini M. et al., 2021, A&A, 649, A169
Stangalini M. et al., 2022, Nat. Commun., 13, 479
Trefethen L. N., 2000, Spectral Methods in MATLAB. SIAM
Trefethen L. N., 2023, Japan J. Ind. Appl. Math., 40, 1587
Van Doorsselaere T. et al., 2020, Space Sci. Rev., 216, 140
Verth G., 2007, Astron. Nachr., 328, 764
Watanabe H., 2014, PASJ, 66, S1
Watanabe H., Kitai R., Ichimoto K., 2009, ApJ, 702, 1048
Yadav R., Mathew S. K., Tiwary A. R., 2017, Sol. Phys., 292, 105
Yadav R., Louis R. E., Mathew S. K., 2018, ApJ, 855, 8
Yuan D. et al., 2023, Nat. Astron., 7, 856

APPENDIX: DETAILS OF THE NUMERICAL SETUP USED TO SOLVE THE EIGENVALUE PROBLEM

A spectral collocation method performs the following operations: collects the given discrete data on the grid points; interpolates the data globally; and evaluates the derivative of the interpolant on the grid points (Trefethen 2023). The solution of the differential equation (25) is written as the sum of orthogonal basis functions whose coefficient must satisfy the differential equation. The discretization of the domain can be carried out by using uniform or non-uniform grids depending upon the problem type. In general, a mathematical problem can be periodic or non-periodic. For periodic problems, equidistant or uniform grid points are of best use but for non-periodic problems, the accuracy of using the regular or uniform grid points is very poor, especially near the boundaries. Therefore, non-periodic functions are generally discretized over irregular or non-uniform grid points such as Chebyshev grid points. The Chebyshev grid points discretize the radial direction in irregular manners bounded between 0 and 1. In this approach, the number of grid points are denser near the boundaries results in better accuracy by better depicting the effect of change due to applied boundary conditions. Such an approach leads to higher accuracy and decreases the code's run time. In the case of equidistant grid points, the discrete data on grid points can be interpolated globally using the trigonometric interpolant (Fourier Spectral method) and for non-uniform grid points, this can be done using Lagrange polynomial interpolant (Chebyshev Spectral method) (Trefethen 2023).

In order to replace the standard Laplacian operator, ∇^2, from polar coordinates to the matrix of Fourier–Chebyshev differentiation, it is important to construct the spectral interpolant and its derivative with generalized independent variables. This can be done by Kronecker products of the differentiation matrices with each of the independent variables. For polar coordinates, studies suggest that the Fourier expansion works best for angular coordinates while Chebyshev expansion is best suited for radial coordinates (Trefethen 2000). Accordingly, the radial coordinate $r \in [0, 1]$ is expanded using Chebyshev expansion, while the angular coordinate $\theta \in [0, 2\pi]$ is expanded using Fourier expansion. This study follows the method developed by Trefethen (2000). An odd number of grid points are selected in the radial direction, while an even number of grid points are selected in the azimuthal direction. As a result, the Laplacian operation becomes

$$L = \left(D_1 + R^{'} E_1\right) \otimes I_l + \left(D_2 + R^{'} E_2\right) \otimes I_r + R^{'2} \otimes D_\theta^{(2)}, \quad \text{(A1)}$$

where D_1 and D_2 are the matrices corresponding to the $\partial^2/\partial r^2$ operator, E_1 and E_2 are the matrices for $(1/r)\partial/\partial r$ and D_θ stands for the $(1/r^2)\partial^2/\partial\theta^2$ operator. In the above expression $R^{'}$ is a diagonal matrix $R^{'} = diag(r_j^{-1})$, $1 \le j \le (N_r - 1)/2$, and I_l and I_r are the identity matrices given by

$$I_l = \begin{pmatrix} I & 0 \\ 0 & I \end{pmatrix}, \quad I_r = \begin{pmatrix} 0 & I \\ I & 0 \end{pmatrix}, \quad \text{(A2)}$$

where I is the $N_{\theta/2} \times N_{\theta/2}$ unit matrix. The matrices in equation (A1) are defined on the grid for Chebyshev collocation points (N_r, odd) and Fourier collocation points (N_θ, even).

After applying the above concepts to the governing equation and after a few simplifications we arrive at the matrix equation that can be used to solve the generalized system of quadratic eigenvalue problem

$$(L + \kappa_0^2) P_{\rm T} - \kappa_0^2 \chi V_{\rm ph}^2 P_{\rm T} = 0. \quad \text{(A3)}$$

In this study, a new algorithm is developed to obtain the eigenvalues and eigenvectors of a quadratic matrix polynomial using QZ factorization. This method is capable of handling a variety of eigenvalue problems in the most efficient way. The method is implemented using MATLAB. In the code, the build-in MATLAB function '$polyeig(L + \kappa_0^2, -\kappa_0^2\chi)$' (which is based on the QZ factorization) is used to obtain the generalized quadratic eigenvalues and eigenvectors. The code is tested against the eigenvalues obtained for the uniform circular cross-sectional-shaped magnetic flux tubes. In

the study by Sathej & Adhikari (2009) the drum head is modelled mathematically as a non-uniform membrane whose density smoothly changes between two predetermined values. They conducted a thorough analysis of the variance in the model's eigenvalues as a function of the model parameters using Fourier–Chebyshev collocation. The eigenspectrum of their model matches the empirically determined eigenvalues of the tabla quite closely. Their code has also been benchmarked against the known eigenvalues of the uniform circular membrane, and they found a spectral convergence as the number of grid points increases. The authors also solved the equations for the eigenvalues and the eigenvectors and using the MATLAB function eigs which is based on a Cholesky decomposition algorithm. In order to achieve spectral convergence, a higher number of grid points is used. A higher number of grid points is also required for obtaining the rapid variation in density over the non-uniform circular cross-sectional shape of the magnetic flux tube especially in radial direction.

This paper has been typeset from a TEX/LATEX file prepared by the author.